

# H<sup>3</sup> (Hydrogel-Based, High-Sensitivity, Hybrid) Plasmonic Transducers for Biomolecular Interactions Monitoring

Bruno Miranda,\* Rosalba Moretta, Principia Dardano, Ilaria Rea, Carlo Forestiere,\* and Luca De Stefano

A hybrid plasmonic transducer made of a Poly-(ethylene glycol) diacrylate (PEGDA) hydrogel and citrate gold nanoparticles detects the biotin-streptavidin interaction at picomolar ( $\times 10^{-12}$  M) concentrations. The all-solution fabrication strategy, herein proposed, is large-scale, easily tunable, and low-cost; nevertheless, this innovative device is highly reproducible and optically stable, and it can be used in dual-optical mode. Indeed, both metal-enhanced fluorescence and localized surface plasmon resonance signals can be exploited to quantify the biorecognition process in a 3D architecture. The large swelling capability of high molecular weight PEGDA is used to investigate the plasmon absorption variations resulting from the exposure to biological solutions containing high molecular weight molecules within the 3D network. The proposed transducer represents a low-cost, flexible, and easy-to-use platform for sensing applications in biomedical or environmental diagnostics.

## 1. Introduction


Point-of-care (POC) and wearable sensing devices based on optical transduction are still in their early stages, mainly due to the very accurate fabrication procedures required and the lower mechanical robustness compared to their electrical/electrochemical analogs.<sup>[1,2]</sup> Nevertheless, new hybrid plasmonic devices based on low-cost, polymeric materials have been recently gaining ground.<sup>[3,4]</sup> Polymers ensure high flexibility, adaptability to nonplanar surfaces, and ease of integration within

more complex systems, such as microelectronics and microfluidics, without compromising high sensitivity and mass production.<sup>[5]</sup> Among the many available polymeric materials, hydrogels represent the ideal substrates for plasmonic sensors due to their optical transparency, biocompatibility, and their swelling capability in presence of an aqueous environment.<sup>[6–8]</sup> Hydrogels are generally recognized as 3D architectures, whose crosslinking density, mesh network size, and polymerization agent can be tuned and selected according to the desired applications. Moreover, they can be easily engineered and made responsive to external stimuli,<sup>[9]</sup> this being crucial when designing analytical platforms with applications in biochemical sensing.<sup>[8,10]</sup>

In this context, when properly assembled and functionalized, noble metal nanoparticles (NPs), basically silver (Ag), and gold (Au), represent the ideal transducers since they can show a dramatically high response upon exposure to a target analyte. In some cases, the transduction is visible to the naked eye, especially in liquid colorimetric assays, which exploit the capability of plasmonic nanoparticles to aggregate, undergoing deep color variations.<sup>[11–13]</sup> Even if very effective and similar to the Enzyme-Linked Immunosorbent Assay (ELISA) commercial kits, the liquid phase plasmonic assays could suffer from pH, ionic strength, and temperature both during the preparation of the assay and the measurement procedure itself.<sup>[14–16]</sup> To overcome these limitations without giving up the sensing advantages provided by plasmonic nanoparticles, both top-down and bottom-up fabrication strategies have been proposed to arrange them in periodic, quasiperiodic, and random arrays on different substrates.<sup>[17–19]</sup> Different transduction mechanisms have been proposed to design plasmonic biochemical sensors and to ensure high sensitivity and specificity. However, portability and ease of use of these optical devices still represent a hard-to-solve challenge. All these transduction mechanisms are based on the localized surface plasmon resonance (LSPR) exhibited by noble-metal NPs.<sup>[20,21]</sup> Refractometric biosensors exploit the LSPR shifts as a function of a target analyte when properly interacting with the biorecognition element adhered on the surface of the NPs;<sup>[22,23]</sup> Surface-enhanced infrared absorption (SEIRA) and surface-enhanced raman scattering (SERS) exploit the LSPR to enhance infrared and Raman signals of molecules onto plasmonic substrates;<sup>[24–26]</sup> Metal-enhanced fluorescence (MEF), also referred to as plasmon-enhanced fluorescence

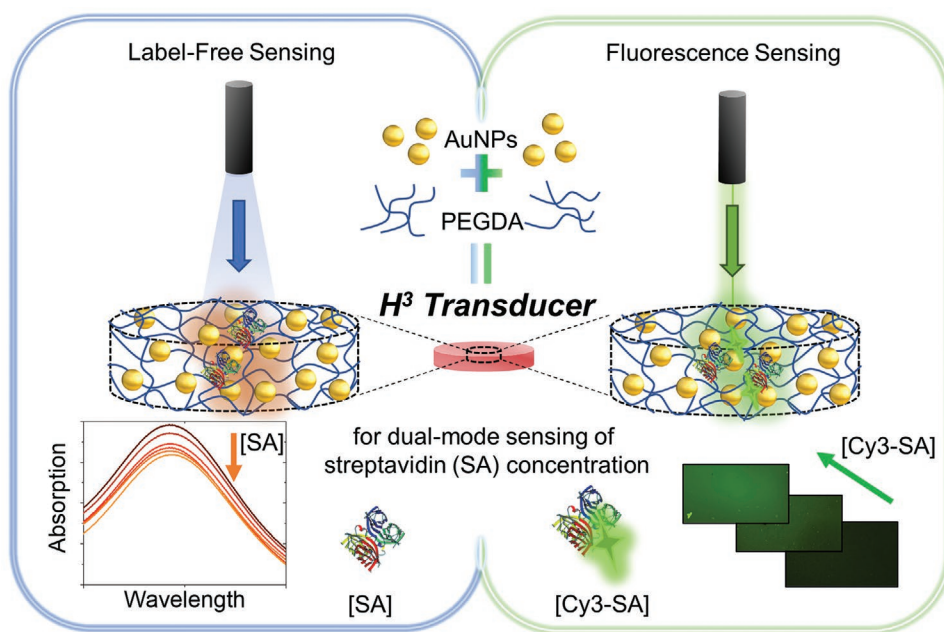
B. Miranda, R. Moretta, P. Dardano, I. Rea, L. De Stefano  
Institute of Applied Sciences and Intelligent Systems  
Unit of Naples  
National Research Council  
Via P. Castellino 111, Napoli 80131, Italy  
E-mail: bruno.miranda@na.isasi.cnr.it

B. Miranda, C. Forestiere  
Department of Electrical Engineering and Information Technology  
University of Naples Federico II  
via Claudio 21, Napoli 80125, Italy  
E-mail: carlo.forestiere@unina.it

 The ORCID identification number(s) for the author(s) of this article can be found under <https://doi.org/10.1002/admt.202101425>.

© 2022 The Authors. Advanced Materials Technologies published by Wiley-VCH GmbH. This is an open access article under the terms of the Creative Commons Attribution License, which permits use, distribution and reproduction in any medium, provided the original work is properly cited.

DOI: 10.1002/admt.202101425



**Scheme 1.** Schematic representation of the plasmonic hydrogel  $H^3$  transducer based on in situ biotinylated AuNPs embedded in PEGDA (10 kDa) for the dual-sensing of nonlabeled and Cy3-labeled streptavidin (SA). In the label-free sensing mechanism, [SA] is monitored by absorption spectroscopy. An increase in the [SA] results in a decrease in the absorption intensity due to the enhanced swelling ratio of the hydrogel. In fluorescence sensing mechanism, [Cy3-SA] is quantified by exploiting the Metal-Enhanced Fluorescence phenomenon arising when the excitation of the fluorescent dye, at distances lower than 10 nm, matches the absorption spectrum of the AuNPs embedded in the hydrogel matrix. The higher [Cy3-SA], the higher the detected fluorescence signal.

(PEF), exploit the LSPR to increase the signal intensity of fluorescent dyes, depending on the spectral overlapping between plasmonic absorption and fluorescent dye extinction/emission and their separation distance.<sup>[27–30]</sup> Moreover, the combination of plasmonic nanoparticles with polymers has been enabling novel functionalities and transduction mechanisms based on the different mechanical properties of flexible substrates.<sup>[15,31–33]</sup> In particular, the synergy between plasmonic nanoparticles and hydrogels has been already shown to be a promising approach for the design of biochemical sensors.<sup>[6,34,35]</sup> We have recently proposed a nanocomposite hybrid material, made of a low-molecular weight (MW) Poly-(ethylene glycol) diacrylate (PEGDA, 700 Da) hydrogel and citrate gold nanoparticles (AuNPs), for biosensing applications. PEGDA was selected due to its optical (it is transparent in the visible), chemical (it is perfectly biocompatible) properties, and mechanical (it exhibits high flexibility and swelling capability) properties.<sup>[36,37]</sup> Moreover, PEGDA was chosen for its ease of use in the fabrication of 3D platforms, which can encapsulate biomolecules, NPs, or nanostructures in a single fabrication step.<sup>[38–40]</sup> Furthermore, we showed that it could mechanically stabilize the AuNPs and ensure a deep contact between them and the target analyte solution.<sup>[22]</sup> PEGDA/AuNPs plasmonic transducers were obtained by mixing AuNPs with a prepolymer solution containing the PEGDA monomers and a photoinitiator (Darocur), then exposing it to UV radiation for  $\approx 1$  min. The result was a flexible transparent film that could be chemically functionalized to selectively interact with a target analyte. The obtained transducer was used as a refractometric sensor by monitoring the LSPR redshift as a function of the target concentration, with a sensitivity up to 110 nm per RIU and a limit of detection (LOD) of  $25 \times 10^{-6}$  M for the biotin,

considered generally as a small molecule.<sup>[22]</sup> The advantages of this system rely on the simplicity of the fabrication approach with two materials (PEGDA and AuNPs), whose chemical and optical properties can be both tailored to specific applications. However, low MW hydrogels exhibit a poor swelling capability, thus limiting their application to small molecules. In this paper, we demonstrate that by increasing the MW of the polymer we can obtain a hydrogel-based, high-sensitivity, hybrid ( $H^3$ ) double optical signal transducer, which can be contemporary used as a label-free optical biosensor and a metal-enhanced fluorescence (MEF) platform even in case of high MW target analytes, such as the streptavidin (SA) molecule. SA is a protein secreted by *Streptomyces avidinii*. It can specifically bind up to four biotin molecules with very high affinity. Biotin/streptavidin interactions are recognized as the strongest noncovalent interactions available in nature and have been extensively employed in the detection of target analytes in biomedical applications.<sup>[41–43]</sup> For this reason, this type of interaction is generally used to prove the applicability of a novel platform in the biosensing field.<sup>[44,45]</sup> We provide a dual-mode optical SA detection strategy based on a flexible, low-cost hydrogel nanocomposite (**Scheme 1**). In particular, the large swelling capability of a high-MW PEGDA (10 kDa) is exploited to monitor the absorption variations of the  $H^3$  transducer as a function of the SA concentration ([SA]) in label-free mode. Indeed, the swelling ratio of the hydrogel is demonstrated to increase as a function of the [SA], with a consequent decrease in the absorption of the AuNPs within the  $H^3$  transducer, achieving a LOD of  $1.6 \times 10^{-9}$  M. Although this result is already competitive with the values reported in the literature, we apply the  $H^3$  transducer also in the MEF mode. In this case, we couple the excitation of a fluorescent dye (Cy3) with the

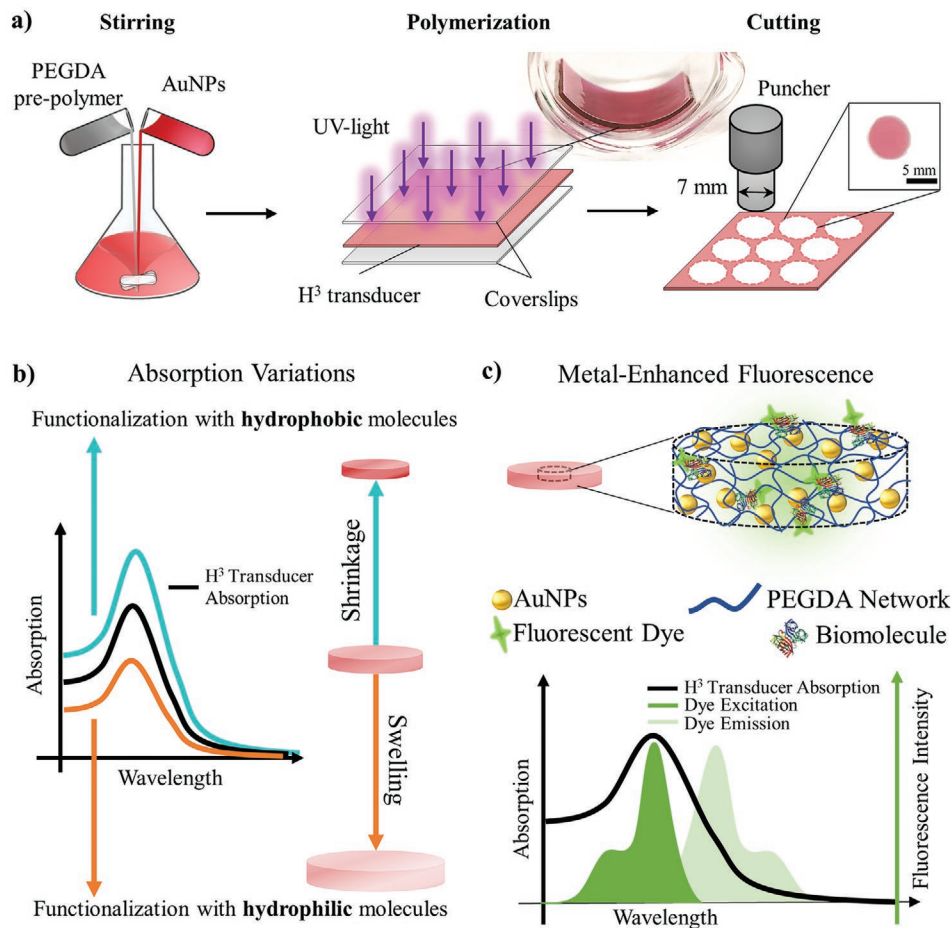


**Figure 1.** a) Schematic representation of the simple fabrication strategy of the plasmonic hydrogel-based ( $H^3$ ) transducers, based on prepolymer solution preparation, photopolymerization, and accurate cutting of the resulting patch. b) Absorption intensity variations due to shrinkage/swelling capability of the hydrogel when the embedded AuNPs are functionalized with hydrophobic/hydrophilic molecules. The functionalization of the  $H^3$  transducer with hydrophobic molecules leads to an increase of the absorption spectrum intensity due to the hydrogel shrinkage (blue line) compared to the bare transducer (black line). On the contrary, the modification of the  $H^3$  transducer with hydrophilic molecules results in a decrease of the absorption spectrum intensity due to the hydrogel swelling (orange line). c) Metal-enhanced fluorescence is obtained by the overlap of the AuNPs absorption and fluorescent dye excitation spectra when the distance between the metal and fluorescent dye is lower than 10 nm. A significant enhancement of the fluorescence can be achieved by immobilizing the labeled-target analyte onto the AuNPs surface within the hydrogel.

absorption of our platform to sense Cy3-SA molecules, showing that a fluorescence enhancement factor (EF) of  $\approx 10$  and a LOD of  $\approx 0.1 \times 10^{-12}$  M can be achieved. The reported EF is obtained by working in excitation mode enhancement, where our non-interacting AuNPs enhance the fluorescence signal of Cy3 in their close proximity (distance  $z < 10$  nm).<sup>[46,47]</sup> These promising results are due to the high reproducibility, flexibility, and stability of our platform and to the possibility of functionalizing the AuNPs directly within the hydrogel matrix, which prevents their spontaneous aggregation or degradation.

## 2. Results and Discussion

### 2.1. Fabrication of Plasmonic $H^3$ Transducers for Dual-Mode Optical Biosensing

The plasmonic  $H^3$  transducer was fabricated following the scheme reported in **Figure 1**. A hydrogel patch was produced

by stirring a prepolymer solution of PEGDA, containing the photoinitiator, with an AuNPs aqueous solution. The resulting suspension was cast between two coverslips and exposed to UV light for a few minutes until complete polymerization. The obtained thin patch ( $24 \times 24$  mm<sup>2</sup>) was cut by a puncher into disks (7 mm in diameter), which were easier to handle and could be functionalized in multiwells with controlled volumes. One run of this process generated nine  $H^3$  transducers, as sketched in **Figure 1a**.

The obtained polymeric patch was transparent, thus allowing straightforward optical characterization in transmission mode. Since we used an all-solution fabrication strategy, this process generated highly reproducible platforms, suitable for large-scale production, whose signal was the typical absorption of plasmonic nanoparticles, as schematized in **Figure 1b**. Although many other fabrication strategies have been shown to obtain plasmonic hydrogel nanocomposites, i.e., in situ metallic salts reduction,<sup>[48]</sup> we chose to directly embed freshly synthesized colloidal NPs within the matrix to guarantee high

homogeneity and good control on the dispersity index of the colloidal suspension before the hydrogel polymerization. From the chemical point of view, the fabricated H<sup>3</sup> transducer was tested in terms of stability at different salt concentrations and pH (Figure S1, Supporting Information), and no degradation of the material was observed nor aggregation or degradation of the AuNPs. From the mechanical point of view, beyond its flexibility and support stability of AuNPs, the high MW PEGDA films revealed a well-detectable swelling (shrinkage) behavior once the AuNPs within the network were functionalized with hydrophilic (hydrophobic) molecules. The two phenomena had opposite effects on the optical properties of the patch, in particular on its absorption (Figure 1b). The LSPR peak at 540 nm, due to the ≈60 nm AuNPs inside the polymeric film, decreased its intensity on swelling, since the number of gold nanoparticles intercepted by the probe light beam, which was kept constant for all the measurements, was diluted in a greater 3D volume. On the contrary, the absorption peak value increased on shrinkage due to AuNPs density increase in a smaller volume (see also Figure S2, Supporting Information). The swelling ratio of the high-MW PEGDA was affected by the hydrophilicity/hydrophobicity of the molecules immobilized on the surface of the AuNPs within the hydrogel, which overall made the effective transducer surface more hydrophilic/hydrophobic, accordingly.<sup>[48,49]</sup> At the equilibrium, after soaking the H<sup>3</sup> platform in water for the washing steps, a decrease in the absorption intensity was observed, together with an increase in the size and swelling ratio of the hydrogel disk in presence of hydrophilic molecules (cysteamine and SA); on the contrary, an increase in the absorption intensity, and a decrease in the size and swelling ratio, in presence of hydrophobic molecules (biotin) were observed, as reported in Figure S3 (Supporting Information). Both the effects were dose-response, i.e., they depended on the concentration of the hydrophilic/hydrophobic molecules used in the functionalization steps and the optical sensing of SA. To further decrease the LOD achieved by the proposed platform and starting from the absorption spectra of the H<sup>3</sup> transducer, we investigated its applicability to MEF in the excitation enhancement mode (Förster Resonance Energy Transfer). In this modality, our transducer could act as a fluorescence enhancer on the condition that matching of its absorption with the excitation of a suitable fluorescent dye was obtained and the distance between them was lower than 10 nm, as schematized in Figure 1c. These preconditions paved the way to the application of the same transducer in two different optical detection modes to monitor biomolecular interactions: one label-free, the other after molecules labeling with a proper emitter. Both mechanisms exploited the optomechanical properties of the nanocomposite arising from the combination of AuNPs and high-MW PEGDA hydrogel. On the one hand, the AuNPs acted as transducing elements and enabled the very well-known functionalization schemes reported in the literature for liquid plasmonic assays, on the other, high MW PEGDA acted as a stabilizer for the AuNPs and as a responsive matrix, allowing the diffusion of the analytes of interest. Moreover, the high flexibility and stretchability of the PEGDA could be exploited for their application to nonplanar substrates (Figure S4, Supporting Information).

## 2.2. Morphological and Optical Characterization of the H<sup>3</sup> Transducers and their Use as MEF Platforms

The AuNPs were synthesized by the seeded-growth method reported in Ref.[50], and after their centrifugation, they were embedded in the PEGDA prepolymer solution. Scanning electron microscopy (SEM) imaging of the AuNPs was performed before (on a flat Si wafer) and after embedding them within the polymeric network (Figure 2a,b, respectively).

The images show that the AuNPs (≈60 nm in size) preserved their spherical shape and homogeneity even after the embedding within the hydrogel (see also Figure S5, Supporting Information). The size of the AuNPs (60 ± 30 nm) was confirmed both in value and in dispersion also by dynamic light scattering (DLS) characterization before their embedding in the hydrogel network, as reported in Figure 2c. The optical characterization of the H<sup>3</sup> transducer was performed in transmission mode, revealing an LSPR peak positioned around 540 nm. The spectroscopic measurements were performed on a minimum of 3 hydrogel disks ( $n \geq 3$ ) per patch obtained independently by applying the fabrication protocol reported in the Experimental Section. The resulting optical signal always confirmed the high reproducibility of the platform. The typical mean absorption spectrum of the H<sup>3</sup> transducer is reported in Figure 2d. All the measurements were obtained after stabilizing the composite metal-polymer patch in demi-water for 24 h, to achieve the full swelling of the freshly fabricated material. The theoretical fit was performed by applying the Mie Theory to an isolated AuNP (60 nm in diameter) surrounded by a medium made of PEGDA and water, which were homogenized at the appropriate ratio.<sup>[21,51]</sup> The assumption of noninteracting nanoparticles held in this case since the interparticle distance within the hydrogel was always lower or comparable to the NPs radius, as confirmed by the SEM images. A very good agreement between the experimental results and the numerical simulation was obtained (see red and blue curves in Figure 2d). In Figure 2e, the excitation/emission spectra of the Cy3 fluorophore, selected for MEF mode, are shown to immediately visualize the spectral overlapping of the fluorescent dye excitation with the absorption of the fabricated transducer. In particular, the fluorescent dye excitation spectrum exhibited two peaks at ≈530 and ≈550 nm, while the H<sup>3</sup> transducer absorption peak fell at ≈540 nm, making Cy3 a suitable candidate for MEF in excitation enhancement mode. Moreover, to be sure that the distance  $z$  between Cy3 and the AuNPs within the hydrogel was lower than 10 nm, SA labeled by Cy3 was selected as the target molecule to prove the sensing approach with MEF. Indeed, the hydrodynamic radius of SA has been reported to be ≈5 nm,<sup>[52]</sup> and, for this reason, even in presence of the biotin small molecule, as a biorecognition element, the value of  $z$  was reasonably expected to be well below 10 nm. On the contrary, for more complex immunoassays involving one or more antibodies, the fluorescence enhancement could be achieved by exploiting the Purcell mechanism, which is based on the coupling of the fluorophore emission with the plasmonic absorption. In this case, great enhancement factors have been observed for values of  $z$  higher than 10 nm.<sup>[28,53]</sup> To experimentally evaluate the possibility of using the hydrogel nanocomposite as a MEF substrate, Cy3-SA (150 × 10<sup>-9</sup> M, 1 mL), was simply diffused

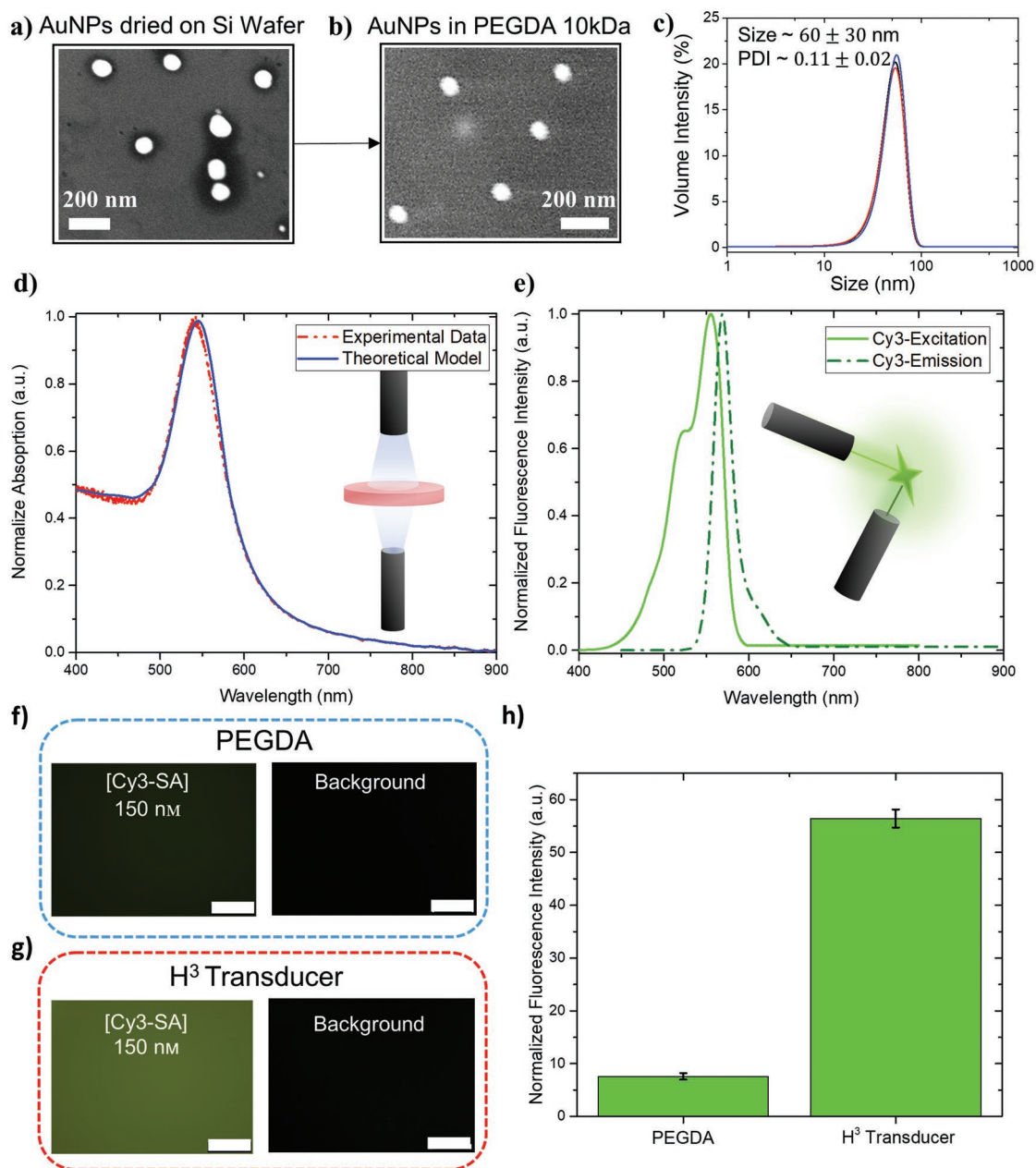


**Figure 2.** SEM micrographs of freshly synthesized AuNPs before a) and after b) embedding in PEGDA hydrogel. No aggregation nor degradation of AuNPs was observed. They preserve their size distribution after their embedding in the hydrogel. c) The size of the AuNPs was confirmed by DLS measurements in water. d) The good agreement between experimental and theoretical absorption spectra of H<sup>3</sup> nanocomposites confirms the hypothesis of noninteracting NPs. e) Fluorescence excitation and emission spectra of the Cy3-SA show a good overlap between Cy3 excitation (peaks at 530 and 550 nm) and H<sup>3</sup> transducer absorption (peak at 540 nm). f) Fluorescence images of PEGDA without AuNPs in presence of Cy3-SA (@150 × 10<sup>-9</sup> M) and its corresponding background. g) Fluorescence images of the H<sup>3</sup> transducer in the presence of Cy3-SA (@150 × 10<sup>-9</sup> M) and its corresponding background. h) Fluorescence intensity counts of Cy3-SA diffused in pure PEGDA and in H<sup>3</sup> transducer to evaluate the fluorescence EF are expressed as mean ± standard deviation (SD) on a minimum of three independent experiments ( $n \geq 3$ ). Scale bars are 250 μm.

overnight into a high-MW PEGDA patch photopolymerized in absence of AuNPs (Figure 2f) and into an H<sup>3</sup> transducer (Figure 2g) having the same physical volume and processing conditions. For this comparison, no functionalization steps were performed since PEGDA without AuNPs did not possess any functional group to be used to link a biorecognition layer for SA. Therefore, we performed this preliminary study on the

enhancement factor (EF) evaluation with no chemical modification of the material. Fluorescence imaging was performed on the two samples (PEGDA and PEGDA/AuNPs nanocomposite) and on their counterpart with nonlabeled SA, in the same conditions, to collect information about the autofluorescence of the material. Fluorescence EF was evaluated as the ratio of fluorescence intensity measured in presence of the AuNPs

and the one measured in absence of the AuNPs, both normalized to their corresponding backgrounds (Figure 2h). An EF of  $\approx 10$  was obtained due to the interaction between the fluorophore and the gold surface of the nanoparticles, compared to the pure PEGDA patch without AuNPs. Moreover, it should be noticed that the  $H^3$  transducers did not suffer from autofluorescence, thus confirming their applicability in fluorescence-based sensing strategies. The optical characterizations and the fluorescence EF determination reported in Figure 2 were exploited for the monitoring of the in situ functionalization of the AuNPs and the selective detection of a target analyte, as reported in Sections 2.3, 2.4, and 2.5.

### 2.3. Chemical Functionalization of the AuNPs within the $H^3$ Transducers

In an optical biosensor, the selectivity, i.e., the ability to quantify a target analyte in a complex mixture such as the blood or another human body fluid, is strictly related to how the transducer surface is decorated with the proper bioprobes, which recognize and interact with the target analyte.<sup>[54,55]</sup> The AuNPs embedded in the  $H^3$  transducer had their surface citrate-terminated according to the process followed for their seeded-growth synthesis.

Therefore, the first step for the chemical functionalization of the platform was thus the substitution of the citrate molecules with a proper linker, the cysteamine, able to bind the bioprobe molecule, in this case, the biotin. Schematized in Figure 3a, the process was developed in situ, acting directly on the AuNPs when embedded into the polymeric layer. Being hydrophilic, cysteamine caused, at the equilibrium, an enhanced swelling ratio of the  $H^3$  transducer, with a consequent decrease in the absorption intensity (Figure 3b). By quantifying the variation of the absorption due to the patch swelling compared to the bare system (denoted as  $|\Delta Abs|$ ), as a function of the cysteamine concentration, the proper amount of the linker was found equal to  $1 \times 10^{-3}$  M. This cysteamine concentration resulted to be the most suitable since saturation was achieved after this value (inset in Figure 3b). After citrate displacement and cysteamine anchoring, the biotin could be covalently bound to the gold surface of the nanoparticles, as reported in the Experimental Section. The hydrophobic nature of the biotin diffused and immobilized inside the  $H^3$  patch (on the AuNPs surface) caused a volumetric shrinkage depending on the biotin concentration (Figure 3c, Supporting Information). The shrinkage was caused by the tendency of the hydrophobic molecule within the hydrogel to repel the aqueous component. Consequently, an increase in the absorption of the  $H^3$  transducer was measured, compared to the absorption of the patch functionalized by cysteamine ( $1 \times 10^{-3}$  M). A titration curve was performed as a function of the biotin concentration and a saturation value was achieved at a biotin concentration of  $4 \times 10^{-3}$  M (inset in Figure 3c). The functionalization of the  $H^3$  transducer was also confirmed by fluorescence microscopy (Figure 3d), using a fixed concentration of Cy3-labeled SA. The dose-response curve reported in the right panel of Figure 3e shows the same saturation behavior of Figure 3c. This result validated the absorption measurements and confirmed the chosen biotin concentration ( $4 \times 10^{-3}$  M) as the most suitable to

achieve the optimal immobilization of the biorecognition layer. The curve in Figure 3e was obtained by measuring the fluorescence of a minimum of three independent  $H^3$  disks ( $n \geq 3$ ) at different biotin concentrations (from  $0 \times 10^{-3}$  M to  $4 \times 10^{-3}$  M) after interaction with the same concentration of Cy3-labeled SA ( $150 \times 10^{-12}$  M). From the same figure, a first control on the specificity of the platform can be also argued. Indeed, no significant fluorescence was observed in absence of biotin, meaning that the nonspecific interaction of the Cy3-SA with the platform was prevented. However, to further reduce nonspecific interactions, a blocking step was added between biotin and streptavidin incubations, as reported in Sections 2.4 and 2.5. Once the best biotin concentration for the functionalization of the AuNPs inside the  $H^3$  patch was fixed, the interaction with solutions having different content of SA was monitored by both LSPR absorption variations and by fluorescence microscopy by using nonlabeled and labeled SA molecules, respectively.

### 2.4. Application of $H^3$ Transducers in Label-Free Sensing of SA

Figure 4a is a schematization of the functionalization approach: the  $H^3$  patch containing biotin modified AuNPs was incubated for 2 h in a BSA solution to block the remaining active sites, which could have been not saturated on the gold surfaces. Then they were soaked in solutions at different concentrations of SA to obtain a dose-response calibration curve of the transducer. In Figure 4b–d, the experimental results are shown. Since SA is a hydrophilic molecule, its biorecognition by the biotin molecules resulted again in an enhancement of the  $H^3$  transducer swelling ratio.

More water permeated inside the hydrogel, thus causing a volume increase of the patch and, as an optical consequence, the decrease of the absorption value measured at the LSPR wavelength (Figure 4b) compared to the patch blocked by BSA. Again, this phenomenon was correlated to the SA concentration ( $[SA]$ ) according to the dose-response curve shown in Figure 4c, from which the sensitivity and the LOD of the platform in the LSPR mode could be quantified.

More precisely, the experimental data were fitted by the common four-parameters Hill equation

$$|\Delta Abs|([SA]) = |\Delta Abs_1| + \frac{|\Delta Abs_2| - |\Delta Abs_1|}{1 + \left(\frac{k}{[SA]}\right)^n} \quad (1)$$

where  $|\Delta Abs_1| = 0.002 \pm 0.001$  (a.u.),  $|\Delta Abs_2| = 0.08 \pm 0.01$  (a.u.),  $k = 6 \pm 1 \times 10^{-9}$  M, and the Hill coefficient  $n = 0.9 \pm 0.2$ . The dynamic range of the  $H^3$  transducer extended from  $1.5 \times 10^{-9}$  M to  $750 \times 10^{-9}$  M, a LOD of  $1.6 \times 10^{-9}$  M was estimated by considering the  $|\Delta Abs|$  threshold as three times the standard deviation (SD) of the control value, while the sensitivity of  $(3.0 \pm 0.3) \times 10^{-3} \times 10^{-9} \text{ M}^{-1}$  could be quantified by considering the linear region of the Hill Curve. Additionally, the negative control experiment and the specificity test are reported in Figure 4d. It was well evident that the functionalized  $H^3$  patch generated a higher response than the patch without biotin on exposure to the highest SA

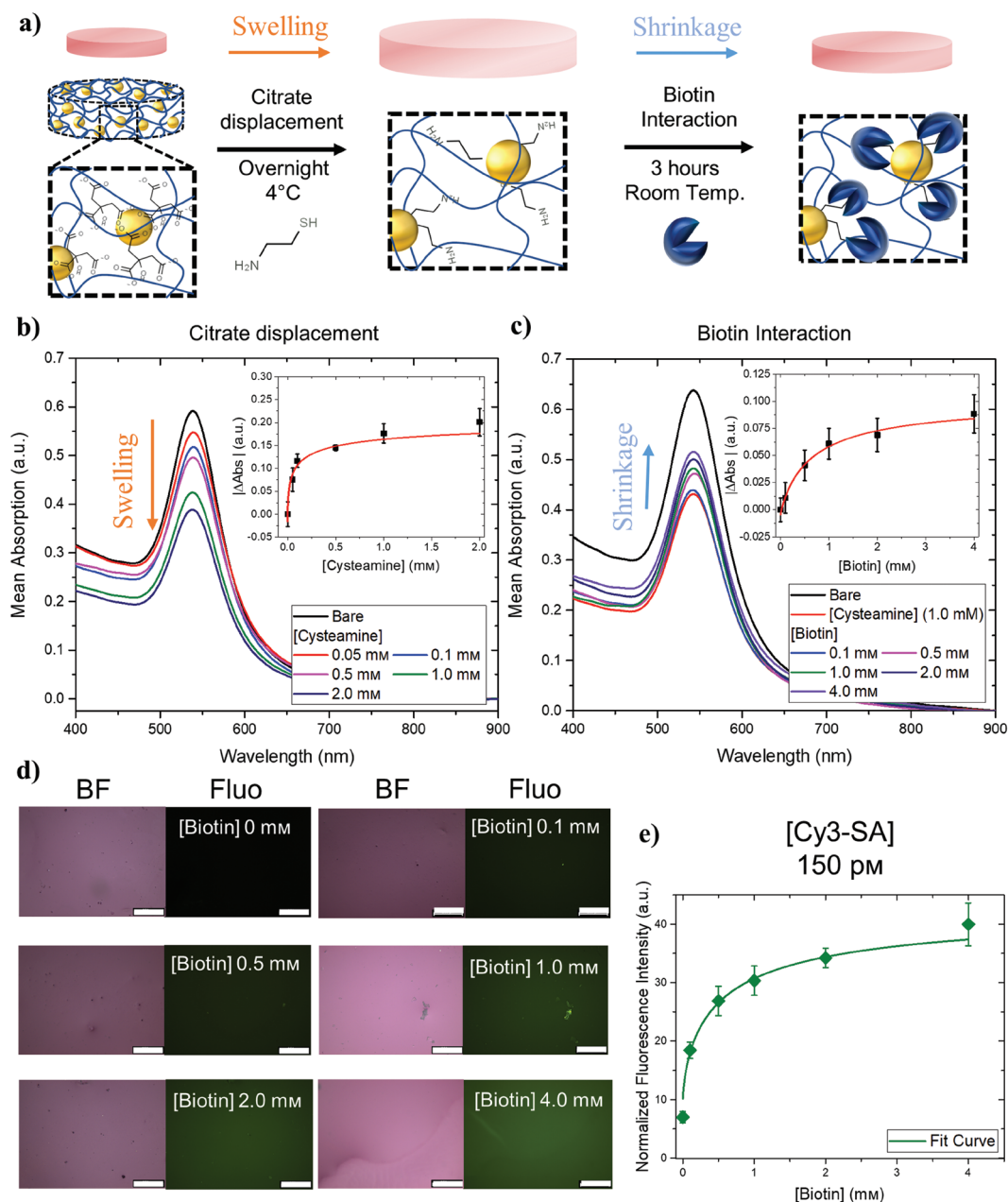


**Figure 3.** a) Schematics of the in situ functionalization approach associated with the swelling ratio variation. Citrate-displacement by cysteamine enables an enhanced swelling ratio, while biotin interaction is responsible for shrinkage of the  $H^3$  transducer. To validate the chemical in situ functionalization of the AuNPs, LSPR measurements were performed. b) Absorption spectra of the  $H^3$  transducer as a function of the cysteamine concentration. In the inset, the absolute value of the mean absorption variation ( $|\Delta Abs|$ ) at  $\lambda_{max}$  against cysteamine concentration (from  $0.05 \times 10^{-3}$  M to  $2.0 \times 10^{-3}$  M) is reported. c) Absorption spectra of the  $H^3$  transducer as a function of the biotin concentration. In the inset, the absolute value of the mean absorption variation ( $|\Delta Abs|$ ) at  $\lambda_{max}$  against biotin concentration (from  $0.1 \times 10^{-3}$  M to  $4.0 \times 10^{-3}$  M), is reported. The optical measurements are obtained from a minimum of three independent samples ( $n \geq 3$ ). SD are reported as vertical bars. d) Validation of the functionalization of the  $H^3$  transducer by fluorescence imaging at a fixed concentration of Cy3-SA ( $150 \times 10^{-12}$  M). Scale bars are 250  $\mu$ m. e) Fluorescence intensity as a function of the biotin concentration on a minimum of three independent images ( $n \geq 3$ ). SD are reported as vertical bars.

concentration ( $750 \times 10^{-9}$  M). An almost four-time percentual variation in the absorption was obtained, thus confirming the effectiveness of the in situ functionalization process. Also, the specificity test performed against a random target, the Protein G (PrG,  $750 \times 10^{-9}$  M), did not lead to significant absorption variation compared to the SA. The results

obtained with the proposed transducer were very promising and competitive with other platforms, which have been recently reported.<sup>[44,45,56–58]</sup> The direct comparison between the results achieved with the  $H^3$  transducer as a novel functional material and the platforms available in the literature for SA sensing is summarized in **Table 1**. The high MW

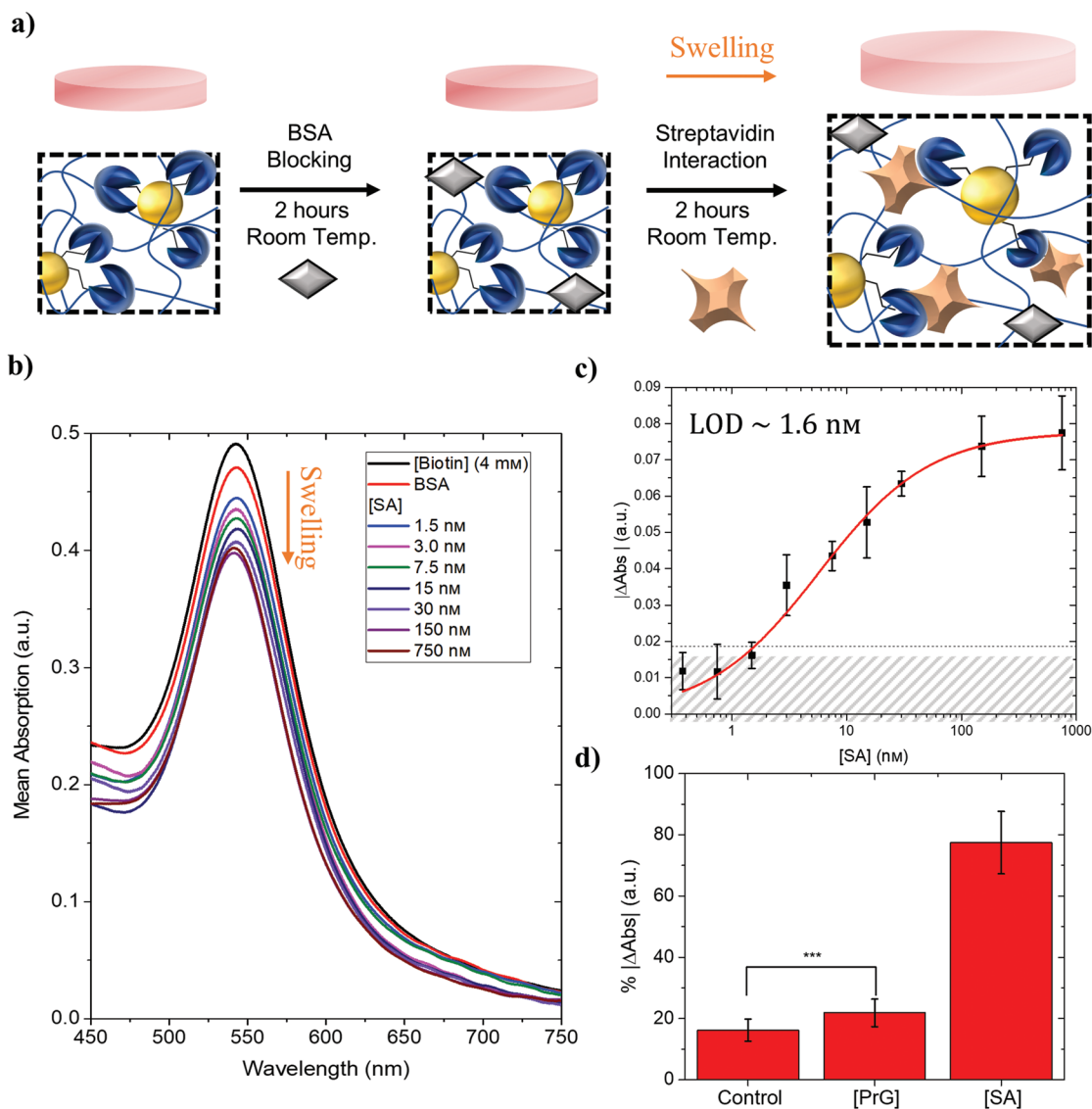


**Figure 4.** Sensing of SA in label-free mode. a) Schematics of the biotin-SA interaction for LSPR sensing associated with the swelling ratio variation. BSA blocking does not cause significant swelling variations, while nonlabeled SA interaction with biotin causes a further increase of the swelling in the H<sup>3</sup> transducer. b) Mean absorption spectra of the H<sup>3</sup> transducer as a function of the SA concentration (from  $0.375 \times 10^{-9}$  M to  $750 \times 10^{-9}$  M). A decrease in the absorption intensity can be observed due to the enhanced swelling of the H<sup>3</sup> transducer as a function of [SA]. c) Absolute value of the mean absorption variation ( $|\Delta Abs|$ ) at  $\lambda_{max}$  is plotted against [SA]. A four-parameters Hill model is used to fit the data. The optical measurements are obtained from a minimum of three independent samples ( $n \geq 3$ ). d) Control and specificity test against a random target (PrG). The control is performed in absence of biotin ( $[SA] = 750 \times 10^{-9}$  M). The specificity test is performed by incubation with PrG ( $[PrG] = 750 \times 10^{-9}$  M). The percent absolute value of the mean absorption variation ( $|\Delta Abs|$ ) at  $\lambda_{max}$  associated with the control and with PrG is monitored and compared with its corresponding value in presence of biotin ( $[SA] = 750 \times 10^{-9}$  M). The experiment is performed on a minimum of three different samples ( $n \geq 3$ ) and the results are reported as mean  $\pm$  SD (reported as vertical bars). \*\*\* $p < 0.001$  resulting from ANOVA test were considered statistically significant.

PEGDA hydrogel combined with AuNPs enabled the design of a simple and efficient platform with a good LOD in label-free mode and a broad dynamic range, which could be mainly ascribed to the 3D nature of our platform. 3D architectures possess, in fact, the advantage of increasing the contact area between the biorecognition element and the target analyte, and this interaction was easily readable by simple spectroscopic measurements due to the swelling capability of the hydrogel and its high transparency.<sup>[59]</sup>

## 2.5. Application of H<sup>3</sup> Transducers as MEF Substrates for Sensing of Fluorescent SA

Since some targets require significantly lower LODs for their suitable quantification, fluorescence spectroscopy is the generally adopted method to boost the sensitivity of many platforms. Moreover, labeling target molecules has become a standardized and straightforward technique for many biomolecules, including DNAs, RNAs, proteins, and aptamers,



**Table 1.** Recently reported methods for the detection of SA.

Method	LOD [ $\times 10^{-9}$ M]	Dynamic range [ $\times 10^{-9}$ M]	Reference
Polymer-based Mach–Zehnder interferometer	1.7	1.7–425	[56]
Low-cost optical cavity	1.4	1.4–190	[45]
Ink-jet printed polymer microdisk laser	1.9	1.9–94	[57]
Poly T-templated copper NPs	0.1	0.5–1000	[58]
LSPR biosensor based on Au nanorods	2.0	2.0–50	[44]
Present work Nonlabeled SA Cy3-SA	1.6 0.0001	1.5–750 0.0001–150	—

and the possibility of sensing tiny concentrations of such molecules by MEF substrates is becoming a very promising strategy in early diagnosis and rapid screening of the population worldwide.<sup>[60–62]</sup> For this reason, based on the previously provided characterizations, we also investigated the sensing performance of the  $H^3$  transducer in MEF mode by using a Cy3-labeled SA as the target element. The results of this analysis are reported in **Figure 5**.

Figure 5a is a schematization of the proposed approach starting from the biotinylated AuNPs within the hydrogel at the optimized biotin concentration reported before. Even in this case, the patch was previously passivated by BSA for minimizing nonspecific interactions and then used for the quantification of different Cy3-SA concentrations. A much lower limit of detection was due to the enhancement of the fluorophore-metallic NPs interaction. The fluorescence images (Figure 5b), which were all acquired in the same experimental conditions (see details in the Experimental Section), were analyzed by ImageJ to derive the fluorescence intensity counts and the dose-response curve (Figure 5c) was obtained by reporting the average counts  $\pm$  SD, of at least three different and independent images for each SA concentration ( $n \geq 3$ ).

The experimental data were fitted by the same standard four-parameters Hill curve, according to the following equation

$$F([SA]) = F_1 + \frac{F_2 - F_1}{1 + \left(\frac{k}{[SA]}\right)^n} \quad (2)$$

where  $F_1 = 0.4 \pm 0.2$  (a.u.),  $F_2 = 56 \pm 3$  (a.u.),  $k = (2.5 \pm 1.2) \times 10^2 \times 10^{-12}$  M and the Hill coefficient  $n = 0.37 \pm 0.04$  are the four fitting parameters. The dynamic range of the  $H^3$  transducer extended in this case from  $0.01 \times 10^{-12}$  M to  $150 \times 10^{-9}$  M, a LOD of  $0.1 \times 10^{-12}$  M resulted by considering the fluorescence threshold as three times the SD of the control value (Figure 5c), while a sensitivity value of  $(8.8 \pm 0.5) \times 10^{-1} \times 10^{-12}$  M<sup>-1</sup> was estimated by considering the linear region of the Hill Curve. Also in the case of MEF measurement, the negative control experiment and the specificity test against a random target (Wheat Germ Agglutinin – WGA protein labeled with Alexa Fluor 555) (Figure 5d) confirmed the relevance of the in situ AuNPs functionalization. When properly biotin-modified, the  $H^3$  patch generated an  $\approx$ ten times higher fluorescence response than

the nonfunctionalized one and the one with a random target. The significantly lower LOD achieved in fluorescence mode was mainly due to the FRET mechanism described earlier, confirming the hypothesized threshold of the fluorophore-NPs distance  $z$  below 10 nm.

### 3. Conclusion

In this work, we proposed a novel and chemically stable hydrogel-based, nanoplasmonic, dual-mode transducer for biochemical sensing applications. The fabrication processes and the materials used are simple and low-cost, thus available to a large community of academic or industrial laboratories. The obtained results demonstrated that simple technologies could give impressive results when properly combined. We showed that a high-MW PEGDA hydrogel enables the generation of a bioresponsive nanocomposite material, whose swelling ratio changed according to the hydrophilicity/hydrophobicity of the molecules used for the AuNPs functionalization. The AuNPs physically entrapped within the hydrogel network act as sensitive transducers of the variations in hydrogel swelling ratio. They follow the hydrogel network swelling or shrinkage and increase or decrease in density, accordingly. We exploited this phenomenon to monitor the hydrogel-based, high-sensitivity, hybrid optical transducer functionalization by monitoring the absorption intensity variations as a function of the streptavidin concentration, as a proof of concept. Moreover, we investigated the well-known metal-enhanced fluorescence phenomenon within the nanocomposite to validate the functionalization scheme and to further improve the performance of the transducer showing a Cy3 fluorescence intensity enhancement of one order of magnitude. We further demonstrated that AuNPs embedded in the hydrogel can be selectively functionalized by a biorecognition element — the biotin — and specifically detect its target analyte — the streptavidin. By building on our results, two approaches could be in principle exploited and even combined to make our transducer of potential impact in biosensing applications: label-free detection strategy, which is based on the mechanical properties of the polymeric network, and MEF-based fluorescence strategy, in which the selection of the fluorescent dye is crucial to achieving ultralow limits of detection. We envisage that this work could pave the way to the design of integrated nanoplasmonic platforms for multiplexed sensing with implications in rapid and low-cost healthcare monitoring, water cleaning, and environmental monitoring. Moreover, the flexible nature of the transducer is also attractive for its inclusion in wearable devices, or portable instrumentation without significant difficulties.

### 4. Experimental Section

**Chemicals and Reagents:** Trisodium citrate ( $Na_3C_6H_5O_7$ ), tetrachloroauric acid ( $HAuCl_4$ ), Poly(Ethylene Glycol) Diacrylate (PEGDA, average Mn 10 000), 2-Hydroxy-2-methylpropiophenone (Darocur 1173), cysteamine, sulfo-*N*-hydroxysuccinimide biotin (biotin-NHS) water-soluble, Bovine Serum Albumin (BSA), Phosphate Buffered Saline (PBS), Tween20, Streptavidin (SA) from *Streptomyces avidinii*, and Streptavidin–Cy3 (Cy3-SA) from *Streptomyces avidinii*, Protein G from *Streptococcus sp.*

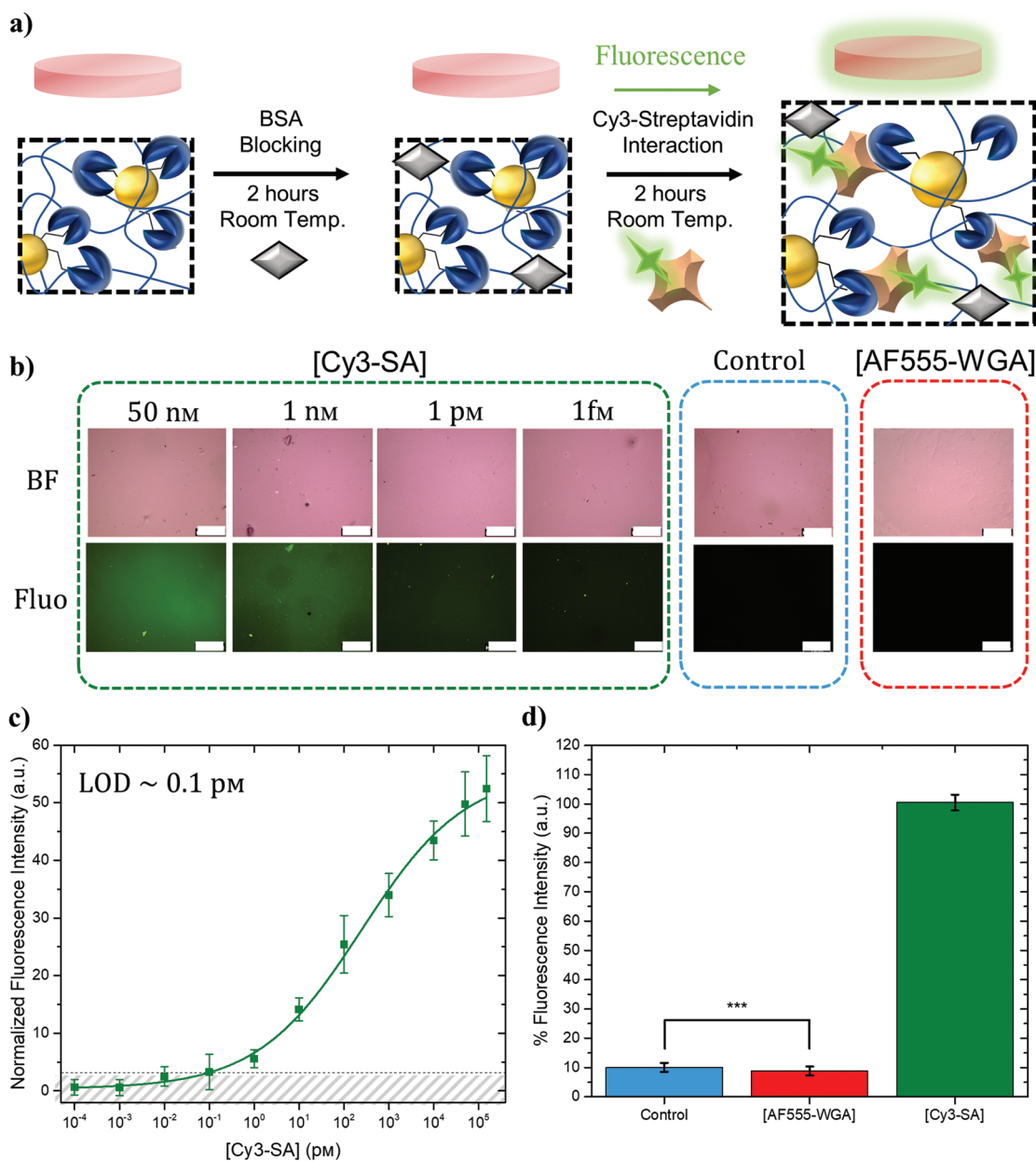


**Figure 5.** Sensing of fluorescent streptavidin (Cy3-SA) by MEF mode. a) Schematics of the biotin-SA interaction for MEF sensing. b) Representative bright-field and corresponding fluorescence images of the H<sup>3</sup> transducer incubated with  $50 \times 10^{-9}$  M,  $1 \times 10^{-9}$  M,  $1 \times 10^{-12}$  M, and  $1 \times 10^{-15}$  M of Cy3-SA (dashed green). The control is performed by incubating Cy3-SA ( $150 \times 10^{-9}$  M) in absence of biotin (dashed blue). The specificity test is performed against a random target (WGA) labeled with a Cy3 equivalent fluorescent dye (AF555) at a concentration of  $150 \times 10^{-9}$  M (dashed red). While for increasing Cy3-SA concentrations an increase in fluorescence intensity is observed, the control and the random target do not show any significant fluorescence. Scale bars are 250 μm. c) The dose-response curve is obtained by measuring the mean  $\pm$  SD of the fluorescence intensity on a minimum of three independent images on three independent samples ( $n \geq 3$ ). A four-parameter Hill model is used to fit the data. A LOD of  $0.1 \times 10^{-12}$  M is achieved. d) The percent fluorescence intensity associated with the control (no biotin and [SA] =  $150 \times 10^{-9}$  M) and with AF555-WGA ( $150 \times 10^{-9}$  M) is monitored and compared with its corresponding value in presence of biotin ([SA] =  $750 \times 10^{-9}$  M). The experiment is performed on a minimum of three different samples ( $n \geq 3$ ) and the results are reported as mean  $\pm$  SD (reported as vertical bars). \*\*\* $p < 0.001$  resulting from ANOVA test were considered statistically significant.

were purchased from Merck KGaA (DE); Wheat Germ Agglutinin (WGA), Alexa Fluor 555 Conjugate was purchased from Thermo Fisher Scientific.

**AuNPs Synthesis and Characterization:** Spherical AuNPs with a controlled size of 60 nm were chemically synthesized by the seed-growth method.<sup>[50]</sup> Briefly, the seed solution was prepared from a trisodium citrate solution ( $2.2 \times 10^{-3}$  M, 150 mL), which was heated up to 100 °C. After boiling incipit, HAuCl<sub>4</sub> (1 mL,  $25 \times 10^{-3}$  M) was added to the

boiling solution to obtain the Au seeds ( $\approx 10$  nm,  $3 \times 10^{12}$  NPs mL<sup>-1</sup>). The solution was cooled down to 90 °C. Then, HAuCl<sub>4</sub> solution (1 mL,  $25 \times 10^{-3}$  M) was injected. The reaction time was set to 30 min, then the injection was repeated. After 30 min, part (55 mL) of the obtained solution was picked up and the remaining part was diluted with MilliQ water (53 mL) and a sodium citrate solution (2 mL,  $60 \times 10^{-3}$  M). The diluted solution represented the new seed for the subsequent

growth step. The synthesis proceeded until the eighth growth step, corresponding to nanoparticles of  $60 \pm 30$  nm ( $PDI = 0.11 \pm 0.02$ ). Since evaporation was prevented during the reaction process, the final volume was kept constant. DLS measurements and UV–vis spectroscopy were performed on the freshly synthesized AuNPs. The DLS size distribution measurements were performed with a Zetasizer Nano ZS (Malvern Instruments, UK) equipped with a HeNe laser (633 nm, fixed scattering angle of  $173^\circ$ ,  $25^\circ\text{C}$ ). The UV–vis absorption spectra were measured by a Cary 100 spectrometer (VARIAN), from 200 to 900 nm.

***H<sup>3</sup> Transducer Fabrication Strategy:*** The freshly synthesized AuNPs were centrifuged at 1920 g at  $10^\circ\text{C}$  for 10 min and concentrated ( $10\times$ ). Poly(ethylene glycol) diacrylate (average Mn 10 000), with Darocur as photoinitiator (1% v/v), was prepared and gently mixed with the concentrated gold nanoparticles in a volume ratio of 2:1, respectively, using a magnetic stirrer at 300 rpm. A volume of 270  $\mu\text{L}$  from each solution was enclosed between two coverslips  $24 \times 24$  mm<sup>2</sup> and photopolymerized by UV-light at 365 nm for 5 min in a UV-exposure box (UV-Belichtungsgerät 2). The final result was a thin hydrogel patch with a thickness of  $\approx 300$   $\mu\text{m}$  embedding AuNPs and having the typical coloration of colloidal AuNPs varying (see Figure 1). Analogously, a prepolymer solution 2:1 PEGDA: MilliQ water was prepared and polymerized in the same conditions. The resulting patch was used as a standard reference for the optical characterizations. The resulting patches were cut in disks with 7 mm diameter by using a puncher, guaranteeing uniform functional area and volume.

***Absorption Spectroscopy:*** The thin hydrogel patches embedding AuNPs were characterized by a customized transmission mode setup at normal incidence. A halogen light source covering the visible and near-IR spectrum (400–900 nm) was connected to a Thorlabs optic fiber conveying light to the sample through a collimator. The transmitted light was collected by another Thorlabs optic fiber connected to a spectrometer (Filmtrics). A schematic representation of the optical setup is reported in Figure 2d. The samples were placed on a coverslip, whose background was removed in the reference measurements. The spectra were collected in the range 400–900 nm with a resolution of  $\approx 0.5$  nm. The absorption of the H<sup>3</sup> Transducer was evaluated by using a pure PEGDA patch (with no AuNPs) as a reference standard. The raw absorption spectra were smoothed to remove noise and the absorption increasing (coupling) and decreasing (decoupling) were evaluated at the peak position ( $\approx 540$  nm). All the measurements were performed by removing the excess water with delicate text wipes to avoid light scattering during the measurements and minimize noise. The size of the collimated light spot conveyed on the samples and the distance between the two optical fibers were kept constant for all the measurements.

***SEM Imaging of AuNPs and H<sup>3</sup> Transducers:*** SEM images have been performed at 5 kV accelerating voltage and 20  $\mu\text{m}$  wide aperture by a Field Emission Scanning Electron Microscope (Carl Zeiss NTS GmbH 1500 Raith FESEM). Secondary Emission and InLens detectors have been used.

***Fluorescence Microscopy and Image Analysis:*** Fluorescence images were acquired by using a Leica AF6000LX-DM6M-Z microscope (Leica Microsystems, Mannheim, Germany), controlled by LAS-X (Leica Application Suite; rel. 3.0.13) software and equipped with a Leica Camera DFC7000T. Both BF and Fluorescence images were acquired by focusing on the hydrogel surface with a  $10\times$  objective. Fluorescence images were obtained by using a Quad-band LED filter cube and setting the excitation filter at 535(25) nm, the dichromatic mirror at 555 nm, and the suppression filter at 575(30) nm. Exposure time and contrast were set at 1.0 s and to 1.0, respectively. Before imaging, the excess water from H<sup>3</sup> transducers exposed to or functionalized with Cy3-SA was removed. A minimum of three images was acquired on three independent samples. The obtained images were analyzed by the ImageJ freeware software by measuring the fluorescence intensity values from fixed regions of interest ( $ROI = 300$  pixels  $\times$  300 pixels). Mean fluorescence intensity values  $\pm$  SD were calculated and normalized according to the minimum and maximum fluorescence values of each measurement session.

***H<sup>3</sup> Transducer Functionalization:*** Before use, the fabricated H<sup>3</sup> transducers were preswollen in MilliQ water for 24 h to remove the

excess Darocur and some eventual unreacted PEGDA. The hydrogel disks were placed in 24-well plates and each reaction was carried out separately. First, they were soaked into a water solution of cysteamine (1 mL) with concentrations varying from  $50 \times 10^{-6}$  M to  $2 \times 10^{-3}$  M (overnight,  $4^\circ\text{C}$ ). After one washing step in a Tween20 buffer (0.2% v/v, 10 min,  $25^\circ\text{C}$ ), to remove the unreacted moieties, and three washing steps in MilliQ water, to restore the swelling equilibrium, the absorption spectra were measured and the variation in the absorption intensity as a function of the cysteamine concentration was analyzed. Second, the covalent interaction of cysteamine-capped AuNPs with biotin was performed by soaking the hydrogel into biotin water solutions (0.25 mL) with concentrations ranging from  $0.1 \times 10^{-3}$  M to  $4.0 \times 10^{-3}$  M (2 h, at room temperature). The same washing steps and optical analysis were performed on the patches to detect the absorption intensity variations to increasing biotin concentrations. A dose-response type equation was used to fit both the absorption intensity decrease as a function of the cysteamine concentration and the absorption intensity increase as a function of the biotin concentration. The variation of the absorption intensity was denoted as the absolute value of the difference of the current absorption intensity compared to the reference value ( $|\Delta Abs|$ ). Then, the H<sup>3</sup> transducers were soaked in a BSA PBS (1x, pH 7.4) solution ( $0.1 \times 10^{-6}$  M, 1 mL) to reduce nonspecific interactions (2 h at room temperature). Finally, fixed volumes (0.25 mL) of PBS solutions of SA (from  $0.375 \times 10^{-9}$  M to  $750 \times 10^{-9}$  M) and Cy3-SA (from  $0.1 \times 10^{-15}$  M to  $150 \times 10^{-9}$  M) with increasing concentrations were incubated in the biotinylated H<sup>3</sup> transducers (2 h at room temperature). The dose-response curves obtained with both SA and Cy3-SA, after the washing steps, were fitted by the four-parameters Hill equation, whose expressions are reported in Equations (1) and (2). The negative controls were performed by incubating SA ( $750 \times 10^{-9}$  M) and Cy3-SA ( $150 \times 10^{-9}$  M), in absence of biotin (2 h at room temperature). The specificity tests were performed by incubating the biotin-modified H<sup>3</sup> transducers with PrG ( $750 \times 10^{-9}$  M) for label-free mode and AlexaFluor555-WGA ( $150 \times 10^{-9}$  M) for MEF mode (2 h at room temperature).

***Numerical Simulations:*** The prediction of the optical response of the H<sup>3</sup> transducer was performed by numerical simulations. The analytical solution of the electromagnetic scattering problem by a spherical nanoparticle, namely, the Mie Theory, was used to perform the simulations.<sup>[51]</sup> At any given frequency, Maxwell–Garnett homogenization theory was applied to evaluate the permittivity of a Gaussian distribution of gold nanoparticles ( $60 \pm 30$  nm) with citrate inclusions, by setting the citrate volume fraction at 10%. The gold optical constants were taken from Johnson and Christy,<sup>[63]</sup> while the citrate refractive index was set to 1.394. The hypothesis of noninteracting nanoparticles was taken into account to predict the experimental absorption spectra. This approximation was made starting from the SEM images, which confirm that the interparticle distance is always less than or comparable with the size of the AuNPs.

The effective medium refractive index was assumed as a weighted average of water and PEGDA optical constants. The refractive index of the polymerized PEGDA (Mn 10 000) with Darocur (1% v/v) was measured by variable angle spectroscopic ellipsometry (SE) (UVISEL, Horiba, Jobin-Yvon). The SE spectra were recorded at three angles of incidence,  $50^\circ$ ,  $55^\circ$ , and  $60^\circ$  in the wavelengths range 400–900 nm with a step of 5 nm.

***Statistical Analysis:*** Mean absorption spectra were calculated as the average of 5 spectra collected on different substrate positions on 10 different samples treated in the same way ( $n \geq 10$ ). The plots of the absorption spectra were obtained by smoothing and, when specified, normalization by using OriginPro 8 free version. The absorption variations  $|\Delta Abs|$  as a function of cysteamine, biotin, and streptavidin concentrations are reported by considering the peak position of the absorption spectra. The mean  $\pm$  SD are representative of at least three independent experiments ( $n \geq 3$ ). For fluorescence analysis, a minimum of 3 images on 3 independent samples was acquired in the same conditions ( $n \geq 3$ ). Fluorescence intensity was evaluated by using ImageJ software. Mean fluorescence intensities were analyzed and normalized by using OriginPro 8. The obtained data are reported as mean  $\pm$  SD. The difference of data

between groups for specificity tests was analyzed by ANOVA by using OriginPro 8 free version.  $p < 0.001$  were considered statistically significant.

Unless otherwise stated, the other data were expressed as mean  $\pm$  SD. SD are reported as vertical bars and are representative of at least three independent experiments ( $n \geq 3$ ).

## Supporting Information

Supporting Information is available from the Wiley Online Library or from the author.

## Acknowledgements

Luca De Stefano acknowledges the partial financial support from CNR @Projects SAC.AD002.173.026 TIPPS (Tracking and Identification of asymptomatic Patients through engineered antibodies bioconjugated plasmonics in a Pandemic Scenario).

Open Access Funding provided by Consiglio Nazionale delle Ricerche within the CRUI-CARE Agreement.

## Conflict of Interest

The authors declare no conflict of interest.

## Data Availability Statement

The data that support the findings of this study are available from the corresponding author upon reasonable request.

## Keywords

biochemical sensing, flexible plasmonics, LSPR, metal-enhanced fluorescence, swelling hydrogels

Received: October 26, 2021

Revised: December 26, 2021

Published online: January 27, 2022

- [1] S. Takaloo, M. Moghimi Zand, *Sens. Bio-Sensing Res.* **2021**, *32*, 100403.
- [2] M. Niazi, E. Alizadeh, A. Zarebkohan, K. Seidi, M. H. Ayoubi-Joshaghani, M. Azizi, H. Dadashi, H. Mahmudi, T. Javaheri, M. Jaymand, M. R. Hamblin, R. Jahanban-Esfahlan, Z. Amoozgar, *Adv. Funct. Mater.* **2021**, 2104123.
- [3] B. C. Simionescu, D. Ivanov, *Handbook of Bioceramics and Biocomposites*, Springer International Publishing, Switzerland **2016**, pp. 233–286.
- [4] L. Li, W. S. Chin, *ACS Appl. Mater. Interfaces* **2020**, *12*, 37538.
- [5] B. Miranda, I. Rea, P. Dardano, L. De Stefano, C. Forestiere, *Biosensors* **2021**, *11*, 107.
- [6] I. Pastoriza-Santos, C. Kinnear, J. Pérez-Juste, P. Mulvaney, L. M. Liz-Marzán, *Nat. Rev. Mater.* **2018**, *3*, 375.
- [7] D. Buenger, F. Topuz, J. Groll, *Hydrogels in Sensing Applications*, Vol. 37, Pergamon, Amsterdam, Netherlands **2012**, pp. 1678–1719.
- [8] J. Bae, J. Park, S. Kim, H. Cho, H. J. Kim, S. Park, D. S. Shin, *J. Ind. Eng. Chem.* **2020**, *89*, 1.
- [9] P. Lavrador, M. R. Esteves, V. M. Gaspar, J. F. Mano, *Adv. Funct. Mater.* **2021**, *31*, 2005941.
- [10] J. Gačanin, C. V. Synatschke, T. Weil, *Adv. Funct. Mater.* **2020**, *30*, 1906253.
- [11] M. Iarossi, C. Schiattarella, I. Rea, L. De Stefano, R. Fittipaldi, A. Vecchione, R. Velotta, B. Della Ventura, *ACS Omega* **2018**, *3*, 3805.
- [12] B. Liu, J. Zhuang, G. Wei, *R. Soc. Chem.* **2020**, *7*, 2195.
- [13] B. Della Ventura, M. Cennamo, A. Minopoli, R. Campanile, S. B. Censi, D. Terracciano, G. Portella, R. Velotta, *ACS Sens.* **2020**, *5*, 3043.
- [14] A. D. Levin, A. Ringaci, M. K. Alenichev, E. B. Drozhzhennikova, K. G. Shevchenko, V. R. Cherkasov, M. P. Nikitin, P. I. Nikitin, *Anal. Bioanal. Chem.* **2020**, *412*, 3423.
- [15] S. Hu, P.-J. J. Huang, J. Wang, J. Liu, *Anal. Chem.* **2020**, *92*, 13354.
- [16] S. Aryal, R. B. Remant, N. Bhattarai, C. K. Kim, H. Y. Kim, *J. Colloid Interface Sci.* **2006**, *299*, 191.
- [17] J. W. Menezes, J. Ferreira, M. J. L. Santos, L. Cesato, A. G. Brolo, *Adv. Funct. Mater.* **2010**, *20*, 3918.
- [18] S.-G. Park, X. Xiao, J. Min, C. Mun, H. S. Jung, V. Giannini, R. Weissleder, S. A. Maier, H. Im, D.-H. Kim, *Adv. Funct. Mater.* **2019**, *29*, 1904257.
- [19] S. Gao, N. Koshizaki, H. Tokuhisa, E. Koyama, T. Sasaki, J.-K. Kim, J. Ryu, D.-S. Kim, Y. Shimizu, *Adv. Funct. Mater.* **2010**, *20*, 78.
- [20] C. Forestiere, A. J. Pasquale, A. Capretti, G. Miano, A. Tamburrino, S. Y. Lee, B. M. Reinhard, L. Dal Negro, *Nano Lett.* **2012**, *12*, 2037.
- [21] L. Wang, M. H. Kafshgari, M. Meunier, *Adv. Funct. Mater.* **2020**, *30*, 2005400.
- [22] B. Miranda, R. Moretta, S. De Martino, P. Dardano, I. Rea, C. Forestiere, L. De Stefano, *J. Appl. Phys.* **2021**, *129*, 033101.
- [23] M. C. Estevez, M. A. Otte, B. Sepulveda, L. M. Lechuga, *Anal. Chim. Acta* **2014**, *806*, 55.
- [24] V. Di Meo, M. Moccia, G. Sanità, A. Crescitelli, A. Lamberti, V. Galdi, I. Rendina, E. Esposito, *Front. Bioeng. Biotechnol.* **2021**, *9*, 666121.
- [25] S. Managò, C. Tramontano, D. D. Cave, G. Chianese, G. Zito, L. De Stefano, M. Terracciano, E. Lonardo, A. C. De Luca, I. Rea, *Small* **2021**, *17*, 2101711.
- [26] H. L. Wang, E. M. You, R. Panneerselvam, S. Y. Ding, Z. Q. Tian, *Light: Sci. Appl.* **2021**, *10*, 161.
- [27] B. Miranda, K.-Y. Chu, P. L. Maffettone, A. Q. Shen, R. Funari, *ACS Appl. Nano Mater.* **2020**, *3*, 10470.
- [28] A. Minopoli, B. Della Ventura, B. Lenyk, F. Gentile, J. A. Tanner, A. Offenhäusser, D. Mayer, R. Velotta, *Nat. Commun.* **2020**, *11*, 6134.
- [29] Y. Jeong, Y. M. Kook, K. Lee, W. G. Koh, *Biosens. Bioelectron.* **2018**, *111*, 102.
- [30] A. Minopoli, A. Acunzo, B. Della Ventura, R. Velotta, *Adv. Mater. Interfaces* **2021**, *2*, 2101133.
- [31] S. Wang, T. Chinnasamy, M. Lifson, F. Inci, U. Demirci, *Trends Biotechnol.* **2016**, *34*, 909.
- [32] A. Mishra, A. R. Ferhan, C. M. B. Ho, J. Lee, D.-H. Kim, Y.-J. Kim, Y.-J. Yoon, *Int. J. Precis. Eng. Manuf. Technol.* **2020**, *8*, 945.
- [33] S. Mariani, A. A. La Mattina, A. Paghi, L. Strambini, G. Barillaro, *Adv. Funct. Mater.* **2021**, *31*, 2100774.
- [34] V. Kozlovskaya, E. Kharlampieva, B. P. Khanal, P. Manna, E. R. Zubarev, V. V. Tsukruk, *Chem. Mater.* **2008**, *20*, 7474.
- [35] I. Willner, *Acc. Chem. Res.* **2017**, *50*, 657.
- [36] S. Lin, N. Sangaj, T. Razafiarison, C. Zhang, S. Varghese, *Pharm. Res.* **2011**, *28*, 1422.
- [37] M. Jamadi, P. Shokrollahi, B. Houshmand, M. D. Joupari, F. Mashhadiabbas, A. Khademhosseini, N. Annabi, *Macromol. Biosci.* **2017**, *17*, 1600479.
- [38] P. Dardano, I. Rea, L. De Stefano, *Curr. Opin. Electrochem.* **2019**, *17*, 121.
- [39] A. Caliò, I. Rea, I. Rendina, J. Politi, L. De Stefano, P. Dardano, *Biomed. Opt. Express* **2016**, *7*, 1645.

- [40] M. Battisti, S. De Martino, B. Miranda, C. Tamaro, P. Dardano, S. Dello Iacono, A. Luca, D. E. Stefano, *Opt. Mater. Express* **2021**, *11*, 2244.
- [41] S. Bearden, F. Wang, A. R. Hall, *Anal. Chem.* **2019**, *91*, 7996.
- [42] T. Lakshmi Priya, S. C. B. Gopinath, T.-H. Tang, *PLoS One* **2016**, *11*, e0151153.
- [43] Y. Yan, T. Hu, X. Xiang, W. Li, C. Ma, *ChemistrySelect* **2021**, *6*, 5248.
- [44] M. Focsan, A. Campu, A. M. Craciun, M. Potara, C. Leordean, D. Maniu, S. Astilean, *Biosens. Bioelectron.* **2016**, *86*, 728.
- [45] D. Rho, S. Kim, *Biosens. Bioelectron.* **2020**, *11*, 4.
- [46] C. D. Geddes, J. R. Lakowicz, *J. Fluoresc.* **2002**, *12*, 121.
- [47] J. R. Lakowicz, C. D. Geddes, I. Gryczynski, J. Malicka, Z. Gryczynski, K. Aslan, J. Lukomska, E. Matveeva, J. Zhang, R. Badugu, J. Huang, *J. Fluoresc.* **2004**, *14*, 425.
- [48] G. R. Deen, V. Chua, *Gels* **2015**, *1*, 117.
- [49] T. B. Alina, V. A. Nash, K. L. Spiller, *Front. Chem.* **2020**, *8*, 593422.
- [50] N. G. Bastús, J. Comenge, V. Puentes, *Langmuir* **2011**, *27*, 11098.
- [51] T. Wriedt, *Mie Theory: A Review*, Vol. 169, Springer, Berlin **2012**, pp. 53–71.
- [52] J. P. Dhandhukia, D. A. Brill, A. Kouhi, M. K. Pastuszka, J. A. MacKay, *Protein Sci.* **2017**, *26*, 1785.
- [53] Ming Li, S. K. Cushing, Nianqiang Wu, *Analyst* **2014**, *140*, 386.
- [54] M. Soler, L. M. Lechuga, *J. Appl. Phys.* **2021**, *129*, 111102.
- [55] Z. Wang, Y. Liu, Z. Wang, X. Huang, W. Huang, *View* **2021**, *6*, 20200165.
- [56] R. Bruck, E. Melnik, P. Muellner, R. Hainberger, M. Lämmerhofer, *Biosens. Bioelectron.* **2011**, *26*, 3832.
- [57] A. Nasir, H. Yoshioka, N. Vasa, R. Yatabe, Y. Oki, Y. Mikami, *Opt. Mater. Express* **2021**, *11*, 592.
- [58] H. B. Wang, H. D. Zhang, Y. Chen, Y. M. Liu, *Biosens. Bioelectron.* **2015**, *74*, 581.
- [59] R. Rebelo, A. I. Barbosa, D. Caballero, I. K. Kwon, J. M. Oliveira, S. C. Kundu, R. L. Reis, V. M. Correlo, *Biosens. Bioelectron.* **2019**, *130*, 20.
- [60] H. Sahoo, *RSC Adv.* **2012**, *2*, 7017.
- [61] C. P. Toseland, *J. Chem. Biol.* **2013**, *6*, 85.
- [62] D. Sun, X. Fan, Y. Shi, H. Zhang, Z. Huang, B. Cheng, Q. Tang, W. Li, Y. Zhu, J. Bai, W. Liu, Y. Li, X. Wang, X. Lei, X. Chen, *Nat. Methods* **2020**, *18*, 107.
- [63] P. B. Johnson, R. W. Christy, *Phys. Rev. B* **1972**, *6*, 4370.